Nanoscale

PAPER

View Article Online
View Journal | View Issue

Cite this: *Nanoscale*, 2025, **17**, 24060

Strategies towards standardizing calibration methods for magnetic particle imaging (MPI) signal quantification: solution *vs.* cellular environments

Elena Ureña Horno, *[a] Mahon L. Maguire, [b] Serbay Ozkan, [c,d] Liam O'Brien, [e] Patricia Murray, [c] Harish Poptani [b,f] and Marco Giardiello *[a]

Magnetic Particle Imaging (MPI) is a powerful technique for non-invasive imaging and iron quantification using superparamagnetic iron oxide nanoparticles (SPIONs), with applications ranging from *in vivo* cell tracking to tracer distribution and biodistribution studies. As the MPI community continues to grow and diversify, there is an increasing recognition of the need for standardized approaches in signal quantification to ensure reproducibility, comparability, and reliable interpretation of results across studies. A key area where standardization is particularly needed is in the construction of calibration curves for quantitative MPI. In this study, we demonstrate that calibration curves derived from SPIONs in solution differ markedly from those obtained in cellular environments. We therefore propose calibrating MPI signal against the number of labelled cells, a strategy that accounts for altered SPION behaviours in the cellular environment and enables more accurate estimation of intracellular iron content. Another critical but often overlooked factor in MPI quantification is the influence of SPION concentration and spatial distribution within the sample. We show that even modest variations in concentration can significantly affect MPI signal intensity, challenging the commonly assumed linear relationship between signal and iron content. Our findings reveal that variations in concentration can introduce nonlinearities in signal response, thereby altering calibration curves and impacting the accuracy and reproducibility of MPI-based quantification. By systematically examining the effects of environmental context and SPION concentration, our study provides a framework for biologically relevant MPI calibration strategies and supports the development of more standardized, reproducible quantification protocols.

Received 17th July 2025,
Accepted 25th September 2025

DOI: 10.1039/d5nr03025k

rsc.li/nanoscale

1. Introduction

Magnetic Particle Imaging (MPI) is an emerging tracer-based imaging modality that enables real-time and quantitative visualization of superparamagnetic iron oxide nanoparticles (SPIONs).[1–3] Unlike anatomical imaging techniques such as MRI,[4] which rely on intrinsic tissue contrast, MPI directly detects SPIONs based on their nonlinear magnetization response to a time-varying magnetic field.[5,6] This response is spatially encoded using a unique mechanism: only SPIONs within a small unsaturated region of the scanner, known as the Field-Free Region (FFR), can dynamically respond to the oscillating drive field and generate signal, while those outside the FFR remain magnetically saturated by the selection field and do not contribute.[6,7] This principle enables highly sensitive and specific detection of tracer distribution. Similar to PET or SPECT, MPI provides quantitative maps of tracer concentration and biodistribution, but without the use of ionizing radiation.[8] These capabilities position MPI as a powerful tool for diverse biomedical applications, including cancer detection, targeted drug delivery, and *in vivo* cell tracking.[9–12]

Traditional MPI signal quantification methods typically rely on calibration curves constructed using SPIONs in solution, based on the assumption that signal response remains consistent across environments. Such an approach overlooks key factors such as interparticle interactions and changes in the SPION magnetic behaviour that can occur when SPIONs are in higher concentration, or when present in complex biological

[a]*Department of Chemistry, University of Liverpool, Liverpool, UK. E-mail: magia@liv.ac.uk*
[b]*Centre for Preclinical Imaging, University of Liverpool, Liverpool, UK*
[c]*Women's and Children's Health Department, Faculty of Health and Life Sciences, University of Liverpool, Liverpool, UK*
[d]*Histology and Embryology Department, Faculty of Medicine, Izmir Kâtip Celebi University, Izmir, Turkey*
[e]*Department of Physics, University of Liverpool, Liverpool, UK*
[f]*Department of Molecular and Clinical Cancer Medicine, University of Liverpool, Liverpool, UK*

contexts such as inside cells. In these environments, SPIONs may aggregate, experience restricted motion, or interact with intracellular structures, all of which can alter their MPI signal characteristics and affect quantification accuracy.

Although SPIONs are frequently considered non-interacting tracers, especially at low concentrations, this assumption often breaks down in biological applications. *In vivo*, particles can accumulate locally in tissues or organs, reaching concentrations where magnetic dipole–dipole interactions between neighbouring SPIONs become significant.[13–16] These interactions can influence MPI signal generation by altering Néel relaxation, which refers to the internal flipping of a particle's magnetic moment and is affected by magnetic coupling, anisotropy, and saturation magnetization.[17] Brownian relaxation, on the other hand, depends on the physical rotation of particles and is primarily influenced by the surrounding medium's viscosity and diffusivity.[18] Aggregation or confinement, such as that occurring in dense or viscous biological environments, can restrict Brownian motion, potentially reducing MPI signal, while magnetic coupling between closely packed particles may induce cooperative effects that enhance it. Thus, the net impact of aggregation on MPI signal depends on the balance between inhibited Brownian relaxation and enhanced magnetic interactions.

This complexity is even more pronounced in cellular environments, where SPIONs are internalized and often immobilized within cellular compartments, such as endosomes or lysosomes, forming dense agglomerates.[19] Within these compartments, SPIONs can also undergo degradation due to the acidic pH and presence of lysosomal enzymes[20,21] which has been shown to unpredictably affect MPI signal intensity depending on nanoparticle composition and degradation pathways.[22] These intracellular processes further restrict Brownian motion and modify magnetic interactions, causing the MPI signal to deviate from a simple linear relationship with iron content. Consequently, accurate interpretation of MPI signals from labelled cells may require calibration approaches that account for these microenvironmental influences.

Solution-based calibration remains a commonly used and practical approach for estimating intracellular iron content in MPI, under the assumption that signal intensity scales consistently with iron mass across different environments.[23–26] While this has enabled substantial progress in the field, this assumption has not been systematically validated in cellular contexts, and its general applicability remains unproven.

As MPI advances toward preclinical and translational applications, there is a growing and recognised need for standardized calibration protocols to improve quantification. Recent initiatives within the field have underscored the importance of consistent acquisition, analysis, the need for reference/calibration samples with matching tissue matrix composition and temperature, and reporting practices to improve reproducibility and enable robust comparisons across studies.[27–31]

In this study, we aim to test whether the linear relationship between MPI signal and iron mass observed in solution-based calibrations remains valid after SPIONs are internalized into cells. Using two widely used tracers, ProMag® and VivoTrax®, we compared calibration curves generated in solution to those derived from MPI signals of labelled cells. This approach allowed us to assess whether factors such as aggregation, confinement, and altered nanoparticle dynamics in the intracellular environment cause deviations from the expected signal response. Our findings reveal significant discrepancies between the two environments, suggesting that standard solution-based calibrations may not reliably quantify intracellular iron. As an alternative, we propose calibrating the MPI signal against the number of labelled cells rather than iron content. This approach not only accounts for intracellular signal alterations, but also bypasses the need to measure the level of cellular labelling, which can vary due to inconsistent uptake and nanoparticle behaviour within cells.

We also evaluate how SPION concentration in solution affects MPI signal intensity. Our results show that even small variations in concentration can lead to substantial changes in signal, despite a constant total iron content. These observations highlight the importance of accounting for dilution effects, particularly when evaluating novel MPI tracers. To explore this, we compare two calibration strategies: the commonly used Fixed Volume approach, widely adopted in MPI and other biological studies, which varies concentration through serial dilution; and a proposed Fixed Concentration method, which maintains a constant SPION concentration while varying sample volume. Our approach minimizes dilution variability and offers a clearer view of the relationship between iron content and MPI signal, preserving intrinsic interparticle interactions. Our findings suggest that Fixed Concentration may provide more reliable calibration by reducing dilution-related variability and avoiding confounding effects associated with concentration-dependent signal changes. To our knowledge, no prior study has systematically investigated solution-based and cellular calibration strategies in MPI, nor examined how effects due to changing concentration by dilution confound quantification. By directly addressing both of these overlooked factors, our investigation aims to introduce a new framework for quantitative MPI calibration.

2. Materials and methods

This study utilized two commercially available SPIONs: ProMag® (PMC1N; Bangs Lab) and VivoTrax® (Magnetic Insight Inc.). The hydrodynamic size (average diameter, D_{ave}), the number-based particle size distribution (D_{num}) and the zeta potential (ζ) were measured at room temperature using a Malvern ZetaSizer Nano ZS equipped with a 4 mW He–Ne laser (633 nm). For size measurements, SPIONs were suspended in deionized water at a concentration of 1 mg mL^{-1}, while zeta potential was assessed in phosphate-buffered saline (PBS, pH 7.4). Iron content was quantified using an Agilent 5110 Inductively Coupled Plasma Optical Emission Spectroscopy (ICP-OES) system. A summary of all characterization data is provided in Table S1.

Sample holder and tube design

To ensure consistent sample positioning within the MPI scanner, a custom 7-well tube holder was used. Flat-bottomed tubes were used to ensure a uniform sample depth across the tube avoiding partial volume issues during subsequent quantitative image analysis. Both the holder and tubes were 3D-printed (Formlabs Form 3) (see Fig. S1, SI). All samples were imaged individually and placed in the same position in the holder (position 3) to ensure consistent ROI selection and to avoid any potential signal contamination that could arise from having multiple samples in the holder.

MPI imaging

Using the Momentum™ MPI system (Magnetic Insight Inc.), 2D MPI images were acquired. The acquisition was performed in high sensitivity mode, utilizing a gradient magnetic field with a strength of 3 T m^{-1}. The system was operated at a fixed frequency of 45 kHz, with drive field amplitudes of 20 and 26 mT along the x and z axes, respectively. The 120 mm (Z) × 60 mm (X) field of view (FOV) was centred on the sample.

Correcting measured images for detector saturation

To address non-linearity in signal response arising from receiver saturation at high SPION concentration, a calibration function was measured (Fig. S2, SI). This function was used to correct measured signal intensities and linearise the signal response at high SPION concentration. Whilst the receiver response at lower SPION concentrations is linear, this correction substantially extends the usable range of the receiver.

ROI analysis methods

To refine our analysis and minimize the influence of background noise, a threshold was applied such that signals below five times the standard deviation (SD) of the noise were excluded from further analysis.[32] Using this threshold, we defined an ROI that captured all voxels with corrected MPI signals exceeding this threshold. ROI extraction and signal quantification were performed using our custom, user-friendly MATLAB script to accelerate MPI image analysis. The script is freely accessible online.[33]

Quantification of sensitivity and resolution

For sensitivity analysis, maximum intensity was calculated as the highest scalar value within the image, and total intensity was determined by multiplying the mean MPI signal (a.u. mm^{-2}) within the ROI by the area of the ROI in mm^2. All calculations were conducted after receiver saturation correction and signal thresholding. Spatial resolution was assessed using the Full Width at Half Maximum (FWHM). Specifically, a profile across the image along the x-direction was placed through the voxel with maximum signal. The profile was fitted with a Lorentzian function and the FWHM in millimetres was calculated.

Cell culture and labelling

Mouse bone marrow mesenchymal stromal cells (MSCs, D1 ORL UVA, CRL-12324) were purchased from the American Type Culture Collection (ATCC). In the initial stage, 1×10^5 MSCs up to passage 15 were seeded into each well of a 12-well plate and incubated overnight under standard culture conditions (5% CO_2, 37 °C). To evaluate the labelling efficiency of ProMag and VivoTrax, the cells were exposed to varying iron concentrations of each particle formulation in complete growth medium DMEM/F12 (Sigma Aldrich-D6546) supplemented with 10% fetal bovine serum (FBS, Gibco, A5256701) and 1% Pen/Strep (Gibco, 15140122) for different time periods ranging from 2 h to 24 h. Following incubation, the labelling solution was removed, and the cells were washed three times with Hanks' Balanced Salt Solution (HBSS, Sigma-Aldrich, H9394), then fixed with 4% paraformaldehyde (Thermo Scientific, 28908) for 20 minutes. The fixed cells were washed twice with PBS, (Gibco, 10010-015). Labelling efficiencies were assessed using a Prussian Blue staining kit (Sigma Aldrich, HT20), followed by quantification of the percentage of stained cells in five randomly selected microscopic fields, each captured at 400× magnification using a Leica DFC420C digital camera. Images were processed using Leica Application Suite software (LAS4.3). Labelling efficiency was defined as the percentage of Prussian Blue–positive cells relative to the total number of cells per field. Results were averaged across the five fields and reported as mean ± standard deviation. Cell viability following SPION labelling was assessed using an ATP-based luminescence assay (CellTiter-Glo, Promega, G7571), which quantifies intracellular ATP levels as an indicator of metabolically active, viable cells.[34–39] After labelling and washing, cells were incubated with CellTiter-Glo reagent on a shaker for 2 minutes, then allowed to stabilize at room temperature for 10 minutes. Luminescence was subsequently measured using a microplate reader (Fluostar Omega), and viability was expressed as a percentage relative to untreated control cells. Results indicated that a 90% labelling efficiency was achieved without compromising cell viability using 15.5 μg Fe per mL ProMag for 2 hours and 240 μg Fe per mL VivoTrax for 3 hours. For MPI analysis, MSCs were seeded in 100 mm Petri dishes at 5×10^4 cells per cm^2. The following day, cells were labelled under these optimized conditions, then washed, trypsinized, and resuspended in HBSS. To prepare the labelled cells for MPI, a series of two-fold dilutions was prepared where cell numbers were reduced by 50% for each dilution, but with a constant volume of 100 μL HBSS. Measurements were made in triplicate with values presented as mean ± standard error of the mean.

Sample preparation for transmission electron microscopy (TEM)

Cells labelled with ProMag or VivoTrax SPIONs were seeded in 6-well plates. After washing ×3 to remove excess particles, they were fixed with 4% paraformaldehyde and 2% glutaraldehyde in 0.1 M cacodylate buffer for 1 hour at room temperature. Cells were then post-fixed with 1% osmium tetroxide for 1 hour, followed by potassium ferrocyanide treatment. After six rinses with double-distilled water, samples were incubated overnight at 4 °C in 0.75% uranyl acetate. Dehydration was carried out using graded ethanol concentrations, followed by progressive infiltration with ethanol–resin mixtures and

embedding in pure resin at 60 °C overnight. Semi-thin sections were used to identify target areas, and 40–50 nm ultra-thin sections were mounted on copper grids. These were stained with 2% uranyl acetate and lead citrate, then imaged using a FEI Tecnai G2 Spirit Bio-TWIN TEM equipped with a Gatan Rio 16 CMOS camera.

Calibration curve construction in solution

Two experimental approaches were employed to construct calibration curves for quantification of SPION content from MPI signal intensities. Fixed-Concentration approach: in this approach, increasing volumes of a stock solution of known concentration were used, ensuring that the SPION concentration remained constant while the total iron mass increased. Fixed-Volume approach: in this approach, samples were prepared as for the Fixed-Concentration approach and were further diluted to fixed final volume, ensuring that each tube contained the same total number of SPIONs as in the Fixed-Concentration approach, but at varying SPION concentration. This approach mirrors the principles of serial dilution, a well-established technique in analytical applications for constructing calibration curves. The Fixed-Volume approach was designed to yield samples with the same total iron mass as those used for the Fixed-Concentration method. This allows for direct comparison between the two methods.

Calibration curve construction in cells – MPI signal *vs.* iron mass

Calibration curves correlating MPI signal intensities with intracellular iron mass were generated using samples containing increasing numbers of iron-labelled cells, where intracellular iron was quantified using ICP-OES. Following MPI measurements, cell pellets were digested in 70% nitric acid for 24 hours to ensure complete digestion of intracellular contents. After digestion, the samples were diluted with deionized water to reduce the acid concentration. The resulting solutions were then analysed for their iron content using the Agilent 5110 ICP-OES system. The MPI signal intensities were plotted against the corresponding iron mass, and a linear regression model was employed to construct the calibration curve for iron mass. Cell numbers were confirmed *via* cell counting.

Calibration curve construction in cells – MPI signal *vs.* cell number

Calibration curves correlating MPI signal intensities with the number of iron-labelled cells were also constructed by preparing a series of cell suspensions with varying cell numbers, confirmed *via* cell counting. MPI signal intensities from each suspension were recorded, and the signal intensities plotted against the corresponding number of cells. A linear regression model was used to construct the calibration curve for cell number, without considering the intracellular iron mass directly.

Calibration curve fitting

Linear regression was applied to the calibration data to derive equations for quantifying unknown iron (Fe) content in future measurements. The regression was deliberately not forced through the origin (0,0) because the signal becomes less precise near the lower detection limit (close to 0 μg Fe) due to equipment noise and error, which could distort the relationship between the MPI signal and iron content.

Data fitting and analysis

Data fitting for linear and Lorenzian models, and calculation of standard errors of the mean, was carried out using Prism (**https://www.graphpad.com**). The coefficient of determination (R^2) is shown for all regression models. Fitting of the receiver gain linearisation was carried using Excel (Microsoft 365) and MPI image gain correction, and thresholding was carried out in Matlab 2024a (Mathworks, USA).

3. Results and discussion

Challenges in translating solution-based MPI calibration to cellular quantification

We first tested whether calibration curves derived from SPIONs in solution can accurately quantify intracellular iron by comparing signal responses from labelled cells with those estimated from solution-based calibration curves. This comparison allowed us to assess whether the standard assumption that MPI signal scales consistently with iron mass across different environments holds true when particles are internalized into cells.

Solution-based calibration curves were first generated for ProMag and VivoTrax using the Fixed-Concentration approach, where increasing volumes were added to achieve a range of known iron masses. MPI signal was measured for each sample using both Maximum Intensity and Total Intensity and plotted against iron mass (Fig. S3, SI). Total Intensity is calculated by multiplying the mean intensity values over the region of interest by the area of the region; *i.e.* this is the sum of all signal within the ROI. Where the ROI encompasses all signal arising from a sample, total intensity is a measure of all signal generated by the sample irrespective of spatial blurring. This differs from quoting the maximum intensity value, which is simply the highest scalar value within an MPI image. It is common in the MPI community to quote MPI signal using these two methods, therefore in this study we opted to present them both.[28] To extend these calibrations to intracellular environments, MSCs were labelled with ProMag and VivoTrax, achieving labelling efficiencies of 96.6 ± 1.1% and 91.5 ± 1.3%, respectively, as confirmed by Prussian Blue staining (Fig. S4, SI). MPI signals were then acquired from increasing numbers of labelled cells, allowing the construction of signal-to-cell number curves (Fig. S5, SI). To quantify intracellular iron content, ICP analysis was performed, enabling the creation of calibration curves that correlate MPI signal with intracellular iron mass (Fig. S6, SI).

Fig. 1b and c compares the MPI calibration curves for ProMag and VivoTrax in solution and in labelled cells, as a function of iron mass, within the same iron content range.

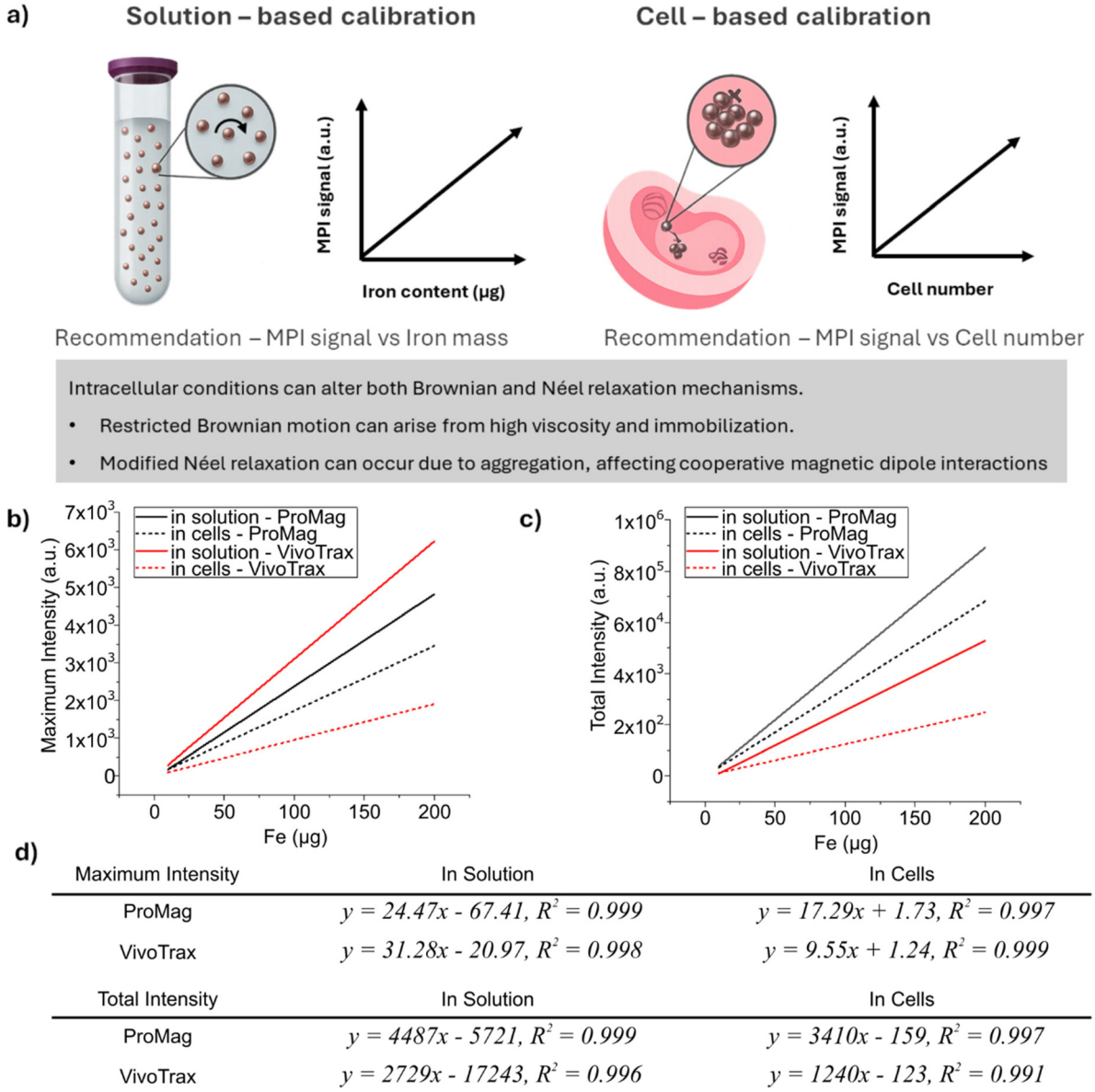

Maximum Intensity	In Solution	In Cells
ProMag	$y = 24.47x - 67.41, R^2 = 0.999$	$y = 17.29x + 1.73, R^2 = 0.997$
VivoTrax	$y = 31.28x - 20.97, R^2 = 0.998$	$y = 9.55x + 1.24, R^2 = 0.999$
Total Intensity	**In Solution**	**In Cells**
ProMag	$y = 4487x - 5721, R^2 = 0.999$	$y = 3410x - 159, R^2 = 0.997$
VivoTrax	$y = 2729x - 17243, R^2 = 0.996$	$y = 1240x - 123, R^2 = 0.991$

Fig. 1 (a) Conceptual overview of calibration strategies for MPI signal quantification. Solution-based calibration is recommended when SPIONs are well-dispersed, while intracellular environments require cell-based calibration due to aggregation and restricted relaxation dynamics. Below, calibration curves for ProMag (black) and VivoTrax (red) in solution (solid lines) and in labelled cells (dashed lines), plotted as a function of iron mass for (b) maximum intensity and (c) total intensity. (d) Summary table of calibration curve parameters for both intensity metrics.

The maximum intensity signal measured in cells falls noticeably below the signal expected based on the corresponding solution-based calibration curves. This discrepancy suggests that applying solution-derived calibrations to labelled cells leads to a systematic underestimation of intracellular iron content. The discrepancy is quantified in Fig. S7 (SI), where the reduction in cellular MPI signal is shown relative to the corresponding signal in solution. For ProMag, the reduction is up to ~30%, while for VivoTrax, it reaches ~70%. A similar trend is observed for total intensity, with reductions of approximately 20% and 50% for ProMag and VivoTrax, respectively. Furthermore, spatial resolution, measured as FWHM, also decreased upon cellular internalization (Fig. S8, SI), with ProMag's resolution decreasing by ~11%, and VivoTrax by ~59%.

The reduced MPI signal observed in labelled cells can be attributed to a substantial decrease in interparticle distance following internalization. In solution, SPIONs remain well-dispersed, whereas in the intracellular environment, they accumulate within confined compartments where they can form dense clusters. Based on estimated calculations (see Tables S2 and S3, SI), the average interparticle distance decreases by orders of magnitude from approximately 116 µm in solution to 306 nm inside cells for ProMag, and from 7.79 µm in solution

to 22.2 nm inside cells for VivoTrax. This close proximity promotes interparticle magnetic interactions and may lead to partial magnetic coupling, which restricts the independent behaviour of individual particles. Combined with the increased viscosity and physical confinement of the intracellular environment, this reduces the ability of SPIONs to dynamically align with the MPI drive field. As a result, the MPI signal intensity of intracellular particles is markedly diminished compared to their well-dispersed counterparts in solution. It is important to note that our study does not seek to compare Promag and VivoTrax to each other, nor to offer a detailed discussion of the probable mechanisms of cellular internalisation for each particle in this cell type, but rather to compare the calibration methods employed. It is interesting to observe, however, that while both nanoparticle types are affected, the underlying mechanisms of internalisation and the impact on signal response differs between ProMag and VivoTrax, which is most likely due to their differences in structure, size, and surface chemistry.

ProMag particles, which consist of micron-sized polymer-encapsulated SPIONs within a fixed matrix, can rotate freely in solution. However, once internalized by cells, the increased intracellular packing density leads to closer proximity between particles, raising the likelihood of physical confinement. This, combined with the high intracellular viscosity and interactions with cellular structures, further limits their rotational freedom. This physical confinement is consistent with TEM observations showing ProMag clustering within endosomal compartments with distinct substructural features (Fig. 2a).

VivoTrax comprises individual SPIONs more susceptible to aggregation and surface modification upon cellular uptake. TEM imaging reveals that VivoTrax nanoparticles predominantly localize as aggregates within endosomes, with some clusters reaching up to 427 nm (Fig. 2b). Additionally, smaller granule-like structures are observed, possibly resulting from partial degradation of the carboxydextran coating in the acidic environment of maturing endosomes and lysosomes.[40] These changes may alter both the stability and magnetic behaviour

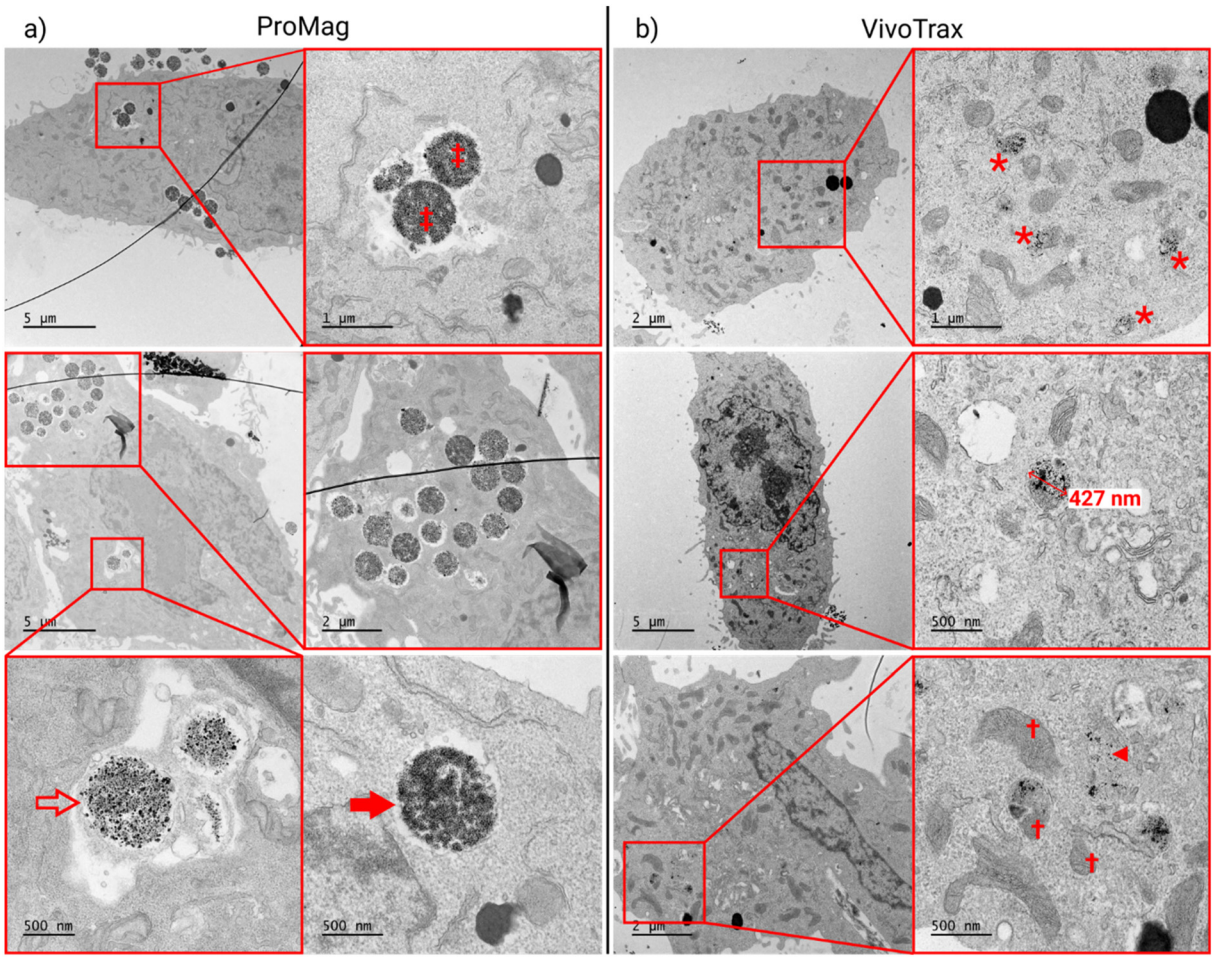

Fig. 2 TEM images of mouse MSCs labelled with (a) ProMag and (b) VivoTrax. ProMag particles form clusters (‡) with distinct substructures: larger granules (open arrow) and smaller granules (solid arrow). VivoTrax particles are localized within endosomes (asterisk; diameter 427 nm), mitochondria (†), and as free cytoplasmic particles (triangle).

of the particles, further limiting their rotational freedom and reducing MPI responsiveness.

Moreover, TEM imaging also revealed occasional isolated nanoparticles present within the cytoplasm, suggesting either partial disruption of endosomal membranes or fusion with cytoplasmic vesicles. Such distribution could arise from endosomal escape, a phenomenon reported for relatively smaller nanoparticles internalized *via* clathrin-mediated or caveolae-mediated endocytosis.[41–44] Interestingly, VivoTrax, but not ProMag, was occasionally observed within mitochondria. This localization could result from mitophagy, whereby damaged mitochondria engulf nanoparticles during degradation, or from passive diffusion following endosomal escape, enabling organelle-specific uptake potentially mediated by the mitochondrial membrane potential.[45]

Overall, our results demonstrate that the MPI signal of intracellular SPIONs deviates significantly from solution-based calibrations due to changes in particle behaviour upon cellular uptake. While these biological effects are important, a detailed mechanistic study of intracellular trafficking is beyond the scope of this work. The key point is that the intracellular environment prevents direct correlation between solution-based calibrations and intracellular MPI signal. In this study, we examined two nanoparticle types of different structure and chemistry, applied to the same cell type, and found that both nanoparticle's behaviour deviated differently from its solution-based equivalent. This demonstrates that no universal correction factor can translate solution-based calibration to cellular MPI signal: each nanoparticle type is affected in a distinct manner, and calibration must therefore be performed on a particle-by-particle, and likely cell type-by-cell type, basis. This highlights the challenge in establishing a reliable correlation between traditional solution-based calibration curves and those for intracellular particles. In light of these findings, we recommend calibrating the MPI signal directly against the number of labelled cells rather than relying on iron mass-based solution calibrations. While this method does not directly quantify iron content, it offers a more accurate link between the MPI signal and intracellular iron. The signal reflects the iron actually internalized by the cells, inherently accounting for intracellular effects such as aggregation, clustering, or changes in nanoparticle dynamics that can alter the MPI signal. This provides more reliable results, particularly for *in vivo* cell tracking, where signal variations could be misinterpreted as differences in cell number, when they may instead reflect changes in SPION dynamics within cells. Additionally, this strategy avoids the need to quantify labelling efficiency, which can vary due to fluctuations in nanoparticle uptake rates across different cell types or conditions, as well as intracellular factors such as aggregation, endosomal trapping, or interactions with cellular components. Because the calibration is directly linked to the number of labelled cells, it bypasses the need to determine the exact iron content per cell, thereby accounting for labelling variability without requiring explicit measurement.

Impact of dilution at constant iron mass

Given that the intracellular environment significantly alters the MPI signal response, we investigated whether similar effects could occur in solution due to changes in SPION concentration. To isolate this effect, we compared MPI measurements from two samples containing the same total iron mass for each nanoparticle type (15.5 μg for ProMag and 10 μg for VivoTrax; difference in masses stem from differences in manufacturer stated concentration, later confirmed by ICP), but redispersed in two different final volumes: 10 μL and 200 μL. This 20-fold dilution allowed us to assess how SPION concentration alone, independent of total iron content, can modulate MPI signal intensity and resolution. The corresponding signal profiles and quantifications are shown in Fig. 3, where black and red lines represent the 10 μL and 200 μL conditions, respectively.

For ProMag, dilution led to a clear reduction in signal: maximum intensity dropped by 9.44%, total intensity by 4.13%, and FWHM broadened by 0.7 mm. These trends indi-

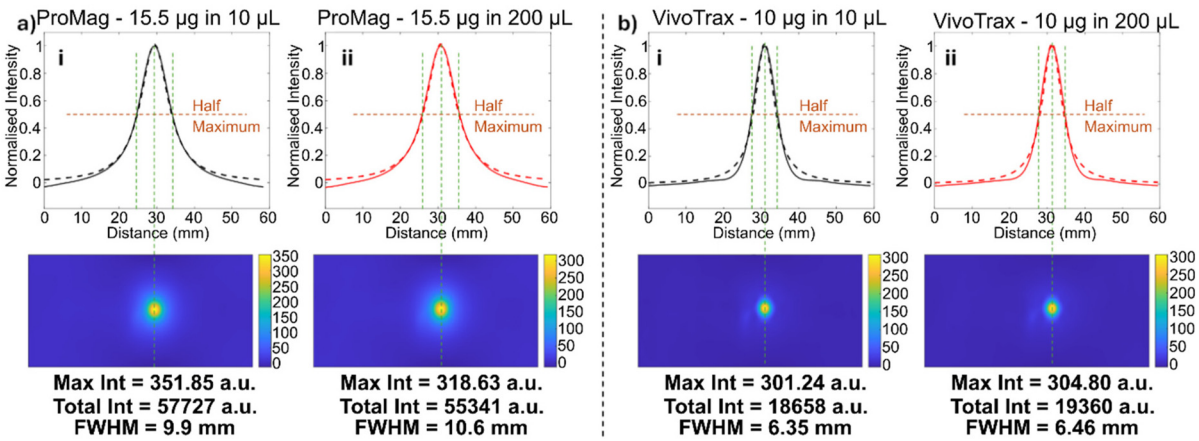

Fig. 3 Comparison of maximum intensities, total intensities, and FWHM values obtained from line profile analysis of MPI images taken for (a) ProMag and (b) VivoTrax samples. The fits show both normalised data (solid lines) and Lorentzian fits (dashed lines). Samples contained 15.5 μg (ProMag) and 10 μg (VivoTrax) of iron redispersed in either 10 μL (black lines) or 200 μL (red lines), corresponding to a 20× dilution.

cate that at lower SPION concentrations, the particles are more spread out, resulting in weaker magnetic interactions between them. This leads to a decrease in signal intensity and a reduction in image sharpness. In addition to modulating interparticle interactions, dilution may also reduce the concentration of stabilizing agents (*e.g.*, coatings or surfactants) that maintain nanoparticle dispersion. Excessive dilution could destabilize SPIONs, leading to aggregation or sedimentation, which may further alter the MPI signal in a nonlinear and unpredictable manner. VivoTrax showed smaller differences between the two conditions. Maximum and Total Intensities changed by −1.18% and −3.76%, respectively, and FWHM increased slightly (0.11 mm). In this context, negative values indicate that the MPI signal was slightly higher in the diluted (200 μL) sample compared to the concentrated (10 μL) one. As mentioned above, it is important to note that this study does not aim to provide a comparison between ProMag and VivoTrax, nor is it intended to provide comparison in terms of their relative suitability for MPI use. As both particles are fundamentally different in terms of structure, hydrodynamic size, and dipole couple, we anticipated that a direct comparison based on their relative masses alone would not be possible. The purpose of the experiments with ProMag and VivoTrax was not direct comparison of their MPI signal magnitudes, but rather to investigate how different calibration approaches perform for each nanoparticle type independently.

Experimental comparison of Fixed-Concentration and Fixed-Volume calibration methods

Building on the observation that SPION concentration influences the MPI signal, we systematically compared two calibration strategies to evaluate how they capture this effect: Fixed-Concentration, where SPION concentration remains constant while iron mass varies, and Fixed-Volume, where a fixed iron mass is diluted to different final volumes, resulting in lower SPION concentrations at each subsequent calibration point (see schematic in Fig. 4a). For the Fixed-Concentration approach, a series of tubes were prepared with increasing volumes of the same stock solution, thereby ensuring a consistent sample concentration with increasing iron mass. To then generate the samples for the Fixed-Volume approach, these same Fixed-Concentration samples were diluted with water to a final volume of 200 μL ensuring an identical iron mass for samples measured in each approach. Three calibrations were performed for each particle type, each starting with a different initial stock solutions of different concentrations: 0.78, 1.55, and 3.1 μg Fe μL^{-1} for ProMag, and 0.5, 1, and 2 μg Fe μL^{-1} for VivoTrax. Iron masses were confirmed by ICP.

MPI measurements revealed systematic differences between the two calibration strategies. For ProMag, both Maximum Intensity and Total Intensity were consistently lower in the Fixed-Volume approach (see Fig. S9, SI) particularly at the lowest concentration, where the sample was approximately 20 times more diluted than the Fixed-Concentration counterpart. Consistent with the concentration-dependent effects observed earlier, the signal reduction likely reflects the impact of weakened interparticle interactions and limited collective magnetic response at lower SPION concentrations. As dilution effects became less pronounced at higher iron contents, the signal differences between the two methods diminished. These trends are reflected in Fig. 4ai and aii, which plot, the percentage difference between the two calibration methods *vs.* the dilution ratios (see eqn (S12)–(S14) SI). The percentage difference in signal between the two methods increased with greater dilution and then plateaued, suggesting that further dilution beyond a certain point has a diminishing effect on the MPI signal, likely due to reduced SPION–SPION interactions. As seen in Fig. 4aiii, we observed that dilution also impacts MPI image resolution. As ProMag concentration decreases in the Fixed-Volume approach, the FWHM values tend to broaden relative to the Fixed-Concentration method, indicating a loss of spatial precision (for further detail refer to Fig. S11a). This suggests that lower ProMag concentrations not only produce weaker signals but also lead to more blurred MPI images. Since total intensity is the integrated intensity over the region of interest, a low resolution increases the signal spread. This helps explain why the Total Intensity does not drop as sharply as Maximum Intensity in diluted samples.

For VivoTrax, differences between calibration methods were less pronounced (see Fig. S10, SI). Maximum intensity remained nearly identical across methods (Fig. 4bi), and Total Intensity was only slightly higher in Fixed-Volume samples (Fig. 4bii), likely due to the same resolution broadening effect observed with ProMag (see Fig. 4biii and Fig. 11b, SI). These findings are consistent with VivoTrax's limited sensitivity to concentration observed in the previous dilution experiments.

These results raised the question of whether the observed differences in MPI signal between the two calibration methods were driven solely by dilution of iron mass or also by magnetic interactions between particles at different concentrations. To explore this further, we conducted a complementary theoretical analysis based on interparticle distance.

Theoretical modelling of interparticle distance effects on MPI signal

Unlike the Fixed-Concentration method, the Fixed-Volume approach introduces variable SPION concentrations between calibration points, and therefore the average distance between particles also varies across the curve. This introduces a potential confounding factor: magnetic interactions between nearby particles may modulate the MPI signal, particularly at higher concentrations where particles are closer together. To evaluate this, we compared the experimental MPI signal from the Fixed-Volume data to theoretical curves that simulate how the signal would scale based solely on interparticle spacing. We estimated the average interparticle distance (d) from SPION concentration and constructed a theoretical signal using the relation:

$$\mathrm{MPI}_{\mathrm{theory}} = \mathrm{MPI}_{\mathrm{ref}} \left(\frac{d_{\mathrm{ref}}}{d} \right)^3 \quad (1)$$

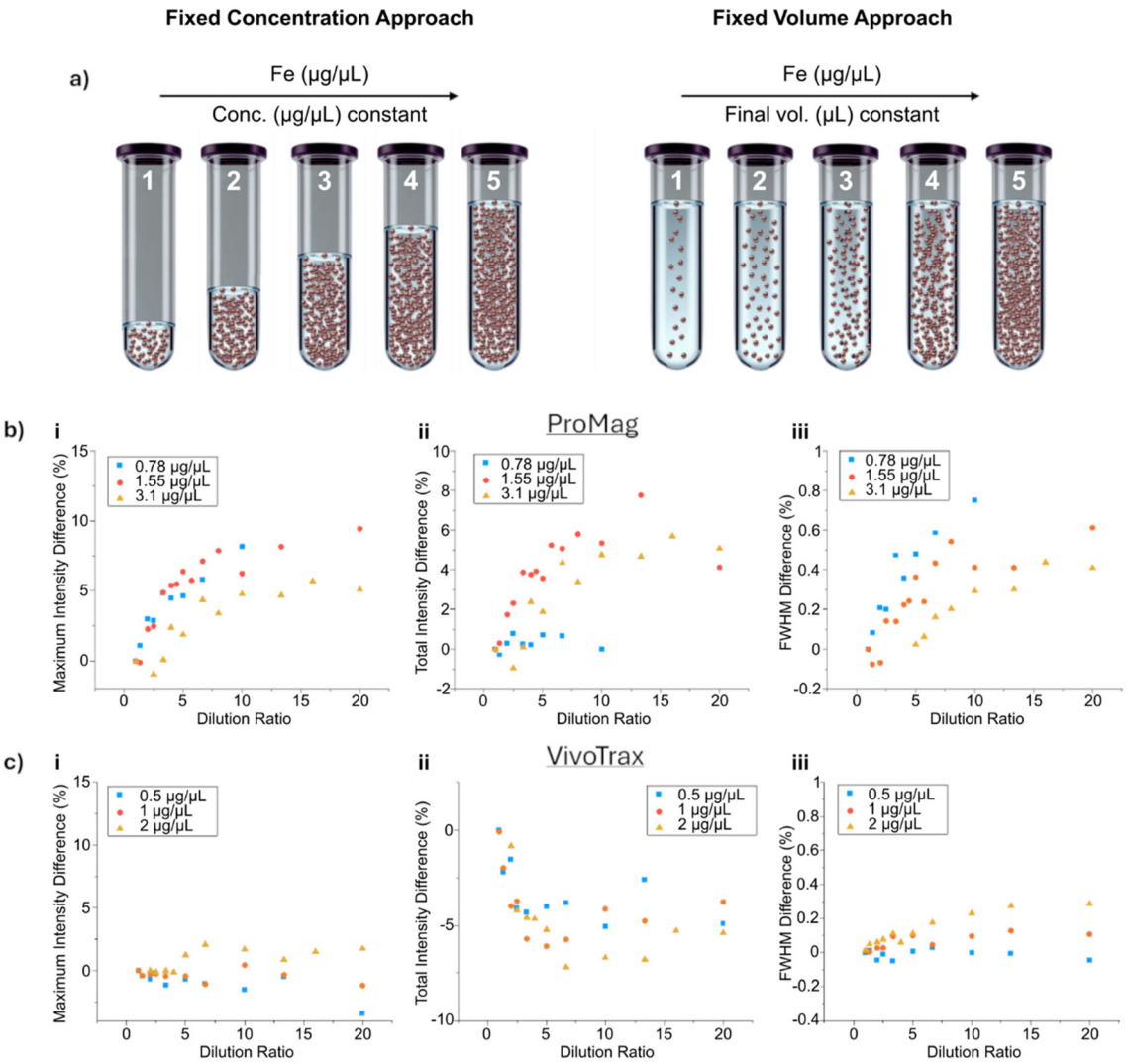

Fig. 4 (a) Schematic illustration of Fixed-Concentration *vs.* Fixed-Volume. (b and c) show comparison of Fixed-Concentration and Fixed-Volume calibration methods for ProMag and VivoTrax expressed as percentage differences between the calibration methods *vs.* dilution ratio; *i.e.* how much the SPION concentration is reduced in the Fixed-Volume sample compared to its Fixed-Concentration counterpart. (bi) Percentage differences in maximum intensity and (bii) percentage differences in total intensity for ProMag across varying dilution ratios. (biii) Shows resolution differences for ProMag, expressed as the change in FWHM. (ci) Percentage differences in Maximum Intensity and (cii) Percentage differences in Total Mean Intensity for VivoTrax across varying dilution ratios. (ciii) Shows resolution differences for VivoTrax, expressed as the change in FWHM. The graph legends indicate the initial stock solutions used to generate each calibration: 0.78, 1.55, and 3.1 μg Fe μL^{-1} for ProMag, and 0.5, 1, and 2 μg Fe per μL^{-1} for VivoTrax. Raw calibration data are presented in Fig. S9, S10 and S11.

where MPI_{theory} represents the predicted MPI signal intensity based on interparticle distance alone, MPI_{ref} is the experimentally measured MPI signal at a reference concentration with corresponding interparticle distance d_{ref} (for derivation of eqn 1, see SI). The variable d denotes the estimated interparticle distance at each tested concentration. This formulation assumes that the MPI signal scales inversely with the cube of the interparticle distance. This model explores how MPI signal would behave if interparticle spacing alone were responsible for signal changes, independent of iron mass or nanoparticle properties.

The resulting theoretical curves (black, Fig. 5) were plotted alongside the experimental MPI signal data from the Fixed-Volume method (Pink squares). It can be observed that the experimental data of maximum intensity consistently lies above the theoretical prediction, especially for ProMag and at shorter interparticle distances (*i.e.*, higher concentrations), with deviations reaching up to ~16% for ProMag and ~5% for VivoTrax. This suggests that MPI signal is not solely governed by the number of particles in a given volume: other effects, such as magnetic coupling or nanoparticle clustering are likely amplifying the response. These additional mechanisms cause the experimental signal to exceed what would be expected from spacing alone. This trend also depends on the signal metric used. Using total intensity (Fig. 5c and d), we observed that both ProMag and VivoTrax experimental data lie above the

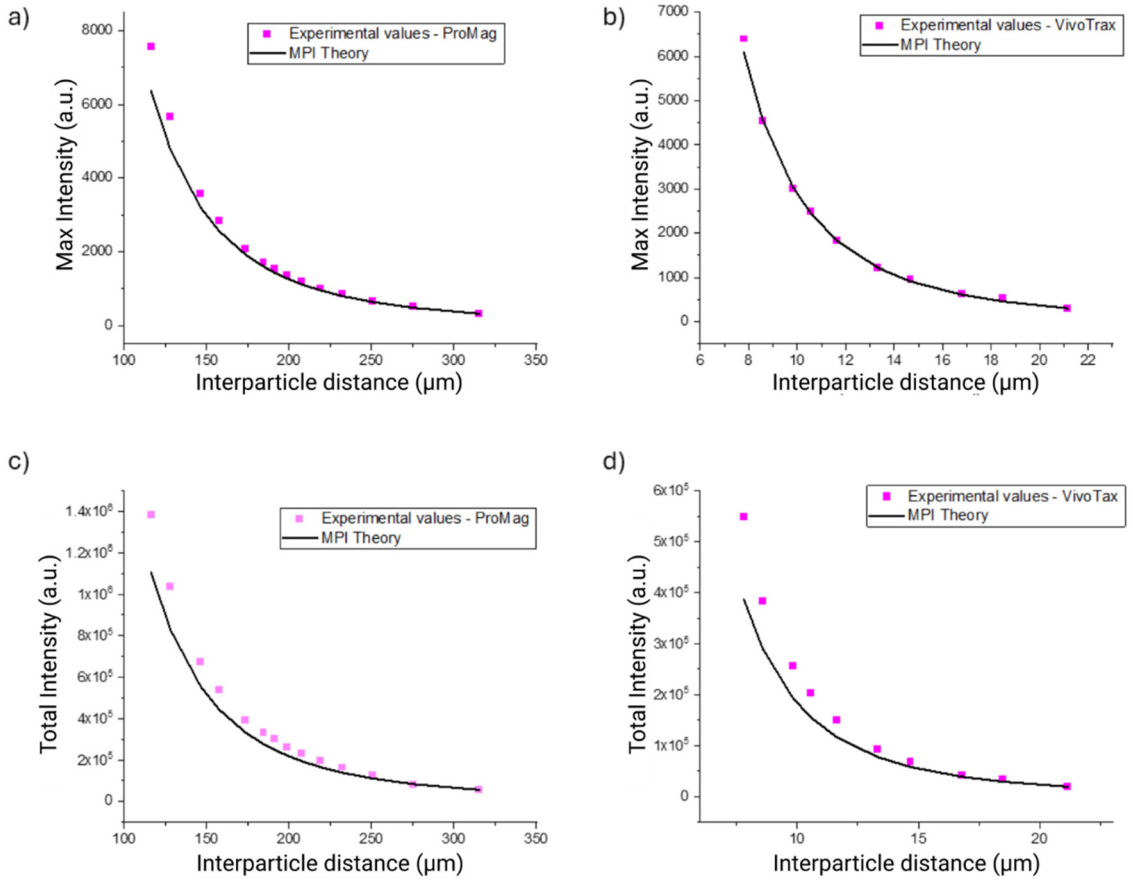

Fig. 5 MPI signal as a function of estimated interparticle distance for ProMag (1.55 μg Fe per μL) and VivoTrax (1 μg Fe per μL) using the Fixed-Volume calibration method. (a and b) Maximum intensity for ProMag and VivoTrax, respectively. (c and d) Total intensity for ProMag and VivoTrax, respectively. Pink squares show experimental MPI signal; black line represents theoretical signal based on interparticle distance estimates.

theoretical curve. With deviations reaching ~20% for ProMag and ~30% for VivoTrax. This indicates that total intensity is influenced by broader phenomena, including spatial signal spread and relaxation dynamics, beyond just interparticle distance.

While the Fixed-Volume approach broadly follows the expected trend, it simultaneously varies iron content and interparticle spacing across the calibration points. This dual dependency introduces nonlinear effects that complicate signal interpretation, as the MPI response can no longer be attributed to iron mass alone. For both SPION types, the experimental signal often deviates from theoretical predictions based solely on spacing, indicating that additional concentration-dependent interactions such as magnetic coupling or clustering play a role. In contrast, the Fixed-Concentration method maintains constant spacing, allowing for more reliable and interpretable calibration based solely on iron mass.

4. Conclusions

We demonstrated that calibration curves derived from particles in solution cannot be directly applied to cellular contexts, as SPION magnetization dynamics are highly dependent on their local environment. For cell-based studies, we recommend calibrating MPI signal as a function of the number of labelled cells rather than iron mass. This approach accounts for intracellular clustering, aggregation, and altered relaxation dynamics, offering a more accurate and biologically relevant method for MPI-based quantification, particularly for *in vivo* cell tracking applications. Moreover, this strategy eliminates the need to quantify labelling efficiency, which can be influenced by variable nanoparticle uptake across different cell types and experimental conditions.

We also show that even small variations in SPION concentration can markedly impact signal intensity, highlighting the importance of carefully controlling and reporting concentration in MPI experiments, specifically for development of novel MPI tracers. As noted by Velazquez-Albino *et al.*[46] standardized characterization and reporting are essential for reliable comparison of novel MPI tracers. While their proposed checklist includes critical physical and magnetic properties, our findings emphasize that SPION concentration, and the resulting interparticle distance, should also be explicitly reported and considered, as it can significantly affect signal output and tracer performance.

Our study showed that concentration-dependent signal variations manifested differently between the two SPIONs tested. Although we evaluated only two types of particles, it is likely that broader differences would emerge with additional SPION formulations or a wider range of concentrations. These findings highlight the need for further investigation and reinforce that particle concentration, reflecting the distribution of SPIONs per unit volume, can influence MPI signal independently of total iron mass. Researchers relying on the classically adopted serial dilution (Fixed-Volume) method may inadvertently build calibration curves that encode not only iron mass but also concentration-dependent interactions, and this sensitivity will vary depending on the SPION used. Additionally, excessive dilution can promote the desorption of surface stabilizers, potentially destabilizing the nanoparticles and contributing to signal variability. To minimize dilution-related effects on MPI signal, we recommend using the Fixed-Concentration calibration method, which maintains a consistent SPION concentration across samples. This strategy enhances reproducibility and supports the reliable comparison of tracer performance, thereby contributing to more robust MPI applications in cellular imaging.

These limitations become even more critical when comparing different SPION formulations or attempting to apply solution-based calibration curves to complex environments such as cells. In such biological contexts, where nanoparticle aggregation, compartmentalization (*i.e.*, the confinement of particles within cellular organelles or regions), and microenvironmental effects further alter MPI signal behaviour, precise and context-specific calibration becomes essential. Our findings reinforce the need to calibrate MPI signals in the same environment where quantification is intended, particularly in cellular systems rather than relying on simplified models based solely on iron mass in solution. Overall, our study provides a foundation for best practices in MPI calibration curve design. By systematically analysing the effects of dilution, SPION concentration, aggregation, and biological compartmentalization, we identify key factors that influence MPI signal behaviour. Recognizing and accounting for these variables will help researchers select appropriate calibration strategies, ultimately improving the accuracy, reproducibility, and biological relevance of MPI-based quantification.

Conflicts of interest

Authors declare no conflict of interest.

Data availability

The data supporting the findings of this study are available within the article and/or its supplementary information (SI). The MATLAB code created by EUH supporting this study is available at **https://doi.org/10.5281/zenodo.15777147**.

Supplementary information is available. See DOI: **https://doi.org/10.1039/d5nr03025k**.

Acknowledgements

We gratefully acknowledge the support of the Liverpool Shared Research Facilities, including the Centre for Pre-Clinical Imaging and the Biomedical Electron Microscopy Facility. We extend our special thanks to Alison Beckett, the facility manager, for her invaluable assistance with the preparation of TEM samples. We also acknowledge funding from UKRI Future Leaders Fellowship (MR/T021306/1 and MR/Y020170/1), the EPSRC (EP/W021579/1) and The Scientific and Technological Research Council of Türkiye (TUBITAK) 2219 International Postdoctoral Research Fellowship Program.

References

1 B. Gleich and J. Weizenecker, *Nature*, 2005, **435**, 1214–1217.
2 S. Harvell-Smith, L. D. Tung and N. T. K. Thanh, *Nanoscale*, 2022, **14**, 3658–3697.
3 B. Rezaei, Z. W. Tay, S. Mostufa, O. N. Manzari, E. Azizi, S. Ciannella, H.-E.-J. Moni, C. Li, M. Zeng, J. Gómez-Pastora and K. Wu, *Nanoscale*, 2024, **16**, 11802–11824.
4 M. A. Bernstein, K. F. King and X. J. O. E. Zhou, *Handbook of MRI Pulse Sequences*, Academic Press, Burlington, 2004.
5 N. Panagiotopoulos, R. L. Duschka, M. Ahlborg, G. Bringout, C. Debbeler, M. Graeser, C. Kaethner, K. Lüdtke-Buzug, H. Medimagh, J. Stelzner, T. M. Buzug, J. Barkhausen, F. M. Vogt and J. Haegele, *Int. J. Nanomed.*, 2015, **10**, 3097–3114.
6 J. Weizenecker, B. Gleich, J. Rahmer, H. Dahnke and J. Borgert, *Phys. Med. Biol.*, 2009, **54**, L1–L10.
7 J. Weizenecker, J. Borgert and B. Gleich, *Phys. Med. Biol.*, 2007, **52**, 6363–6374.
8 P. W. Goodwill and S. M. Conolly, *IEEE Trans. Med. Imaging*, 2011, **30**, 1581–1590.
9 X. Y. Zhou, Z. W. Tay, P. Chandrasekharan, E. Y. Yu, D. W. Hensley, R. Orendorff, K. E. Jeffris, D. Mai, B. Zheng, P. W. Goodwill and S. M. Conolly, *Curr. Opin. Chem. Biol.*, 2018, **45**, 131–138.
10 O. C. Sehl, J. J. Gevaert, K. P. Melo, N. N. Knier and P. J. Foster, *Tomography*, 2020, **6**, 315–324.
11 E. Y. Yu, M. Bishop, B. Zheng, R. M. Ferguson, A. P. Khandhar, S. J. Kemp, K. M. Krishnan, P. W. Goodwill and S. M. Conolly, *Nano Lett.*, 2017, **17**, 1648–1654.
12 Z. W. Tay, P. Chandrasekharan, B. D. Fellows, I. R. Arrizabalaga, E. Yu, M. Olivo and S. M. Conolly, *Cancers*, 2021, **13**, 5285.
13 Z. W. Tay, S. Savliwala, D. W. Hensley, K. L. B. Fung, C. Colson, B. D. Fellows, X. Zhou, Q. Huynh, Y. Lu, B. Zheng, P. Chandrasekharan, S. M. Rivera-Jimenez, C. M. Rinaldi-Ramos and S. M. Conolly, *Small Methods*, 2021, **5**, e2100796.

14 G. Barrera, P. Allia and P. Tiberto, *Nanoscale*, 2021, **13**, 4103–4121.
15 E. Teeman, C. Shasha, J. E. Evans and K. M. Krishnan, *Nanoscale*, 2019, **11**, 7771–7780.
16 S. Mørup, M. F. Hansen and C. Frandsen, *Beilstein J. Nanotechnol.*, 2010, **1**, 182–190.
17 L. Néel, *Ann. Geophys.*, 1949, **5**, 99–136.
18 A. Einstein, *Investigation on the theory of the Brownian movement*, Courier Corporation, 1956.
19 U. M. Engelmann, J. Seifert, B. Mues, S. Roitsch, C. Ménager, A. M. Schmidt and I. Slabu, *J. Magn. Magn. Mater.*, 2019, **471**, 486–494.
20 N. Nelson, J. Port and M. Pandey, *J. Nanotheranostics*, 2020, **1**, 105–135.
21 Y. Portilla, V. Mulens-Arias, A. Paradela, A. Ramos-Fernández, S. Pérez-Yagüe, M. P. Morales and D. F. Barber, *Biomaterials*, 2021, **28**, 121365.
22 J. Guzy, S. Chakravarty, F. J. Buchanan, H. Chen, J. M. Gaudet, J. M. L. Hix, C. L. Mallett and E. M. Shapiro, *ACS Appl. Nano Mater.*, 2020, **3**, 3991–3999.
23 O. C. Sehl and P. J. Foster, *Sci. Rep.*, 2021, **11**, 22198.
24 R. J. Williams, O. C. Sehl, J. J. Gevaert, S. Liu, J. J. Kelly, P. J. Foster and J. A. Ronald, *Tomography*, 2023, **9**, 178–194.
25 P. Chandrasekharan, K. L. B. Fung, X. Y. Zhou, W. Cui, C. Colson, D. Mai, K. Jeffris, Q. Huynh, C. Saayujya, L. Kabuli, B. Fellows, Y. Lu, E. Yu, Z. W. Tay, B. Zheng, L. Fong and S. M. Conolly, *Nanotheranostics*, 2021, **5**, 240–255.
26 A. Shakeri-Zadeh, C. Wang, S. Kuddannaya, S. Yousf and J. W. M. Bulte, bioRxiv, 2025, preprint, DOI: **10.1101/2025.04.16.649154**.
27 H. Poptani, L. O'Brien and M. Giardiello, *Matter*, 2024, **7**, 2718–2720.
28 H. J. Good, O. C. Sehl, J. J. Gevaert, B. Yu, M. A. Berih, S. A. Montero, C. M. Rinaldi-Ramos and P. J. Foster, *Mol. Imaging Biol.*, 2023, **25**, 954–967.
29 M. O. Pacheco, I. K. Gerzenshtein, W. L. Stoppel and C. M. Rinaldi-Ramos, *Adv. Healthcare Mater.*, 2024, **13**, e2400612.
30 J. Tashkandi, R. Brkljača and K. Alt, *Nanoscale Adv.*, 2023, **5**, 4873–4880.
31 M. Salimi, W. Wang, S. Roux, G. Laurent, R. Bazzi, P. Goodwill, G. Liu and J. W. M. Bulte, *Nanoscale Adv.*, 2025, **7**, 1018–1029.
32 O. C. Sehl, B. Tiret, M. A. Berih, A. V. Makela, P. W. Goodwill and P. J. Foster, *bioRxiv*, 2022, preprint, DOI: **10.1101/2022.04.10.487778**.
33 E. Ureña Horno, *Zenodo*, 2025, preprint,DOI: **10.5281/zenodo.15777147**.
34 T. L. Riss, R. A. Moravec, A. L. Niles, H. A. Benink, T. J. Worzella and L. Minor, *Assay Guidance Manual*, NIH, 2013 (updated 2016).
35 R. Hachani, M. A. Birchall, M. W. Lowdell, G. Kasparis, L. D. Tung, B. B. Manshian, S. J. Soenen, W. Gsell, U. Himmelreich, C. A. Gharagouzloo, S. Sridhar and N. T. K. Thanh, *Sci. Rep.*, 2017, **7**, 7850.
36 G. A. F. van Tilborg, D. P. Cormode, P. A. Jarzyna, A. van der Toorn, S. M. A. van der Pol, L. van Bloois, Z. A. Fayad, G. Storm, W. J. M. Mulder, H. E. de Vries and R. M. Dijkhuizen, *Bioconjugate Chem.*, 2012, **23**, 941–950.
37 A. L. M. Jasmin, L. Torres, L. Jelicks, A. C. C. de Carvalho and R. Mendez-Otero, in *Methods in Molecular Biology*, ed. C. Modo, Humana Press, Totowa, NJ, 2012, vol. 906, pp. 239–252.
38 A. S. Arbab, E. K. Jordan, L. B. Wilson, G. T. Yocum, B. K. Lewis and J. A. Frank, *Hum. Gene Ther.*, 2004, **15**, 351–360.
39 J. W. M. Bulte, T. Douglas, B. Witwer, S.-C. Zhang, E. Strable, B. K. Lewis, H. Zywicke, B. Miller, P. Van Gelderen, B. M. Moskowitz, I. D. Duncan and J. A. Frank, *Nat. Biotechnol.*, 2001, **19**, 141–147.
40 J. Huotari and A. Helenius, *EMBO J.*, 2011, **30**, 3481–3500.
41 N. Oh and J. H. Park, *Int. J. Nanomed.*, 2014, **9**, 51–63.
42 F. Toscano and M. Torres-Arias, *Curr. Res. Immunol.*, 2023, **4**, 100073.
43 S. H. Lee, D. J. Park, W. S. Yun, J. E. Park, J. S. Choi, J. Key and Y. J. Seo, *J. Controlled Release*, 2020, **10**, 408–418.
44 M. Lévy, F. Lagarde, V.-A. Maraloiu, M.-G. Blanchin, F. Gendron, C. Wilhelm and F. Gazeau, *Nanotechnology*, 2010, **21**, 395103.
45 X. Liu, M. Li and S. Woo, *Pharmaceutics*, 2024, **16**, 1167.
46 A. C. Velazquez-Albino, E. D. Imhoff and C. M. Rinaldi-Ramos, *Sci. Adv.*, 2025, **11**, eado7356.